Topological states in breathing honeycomb plasmonic nanoparticle arrays with in-plane polarized modes

Huizhou Wu*

College of Electronic and Information Engineering, Harbin Institute of Technology (Shenzhen), Shenzhen 518055, China

(Received 12 May 2023; accepted 4 January 2024; published 5 February 2024)

In this paper, we investigate the topological properties of breathing honeycomb plasmonic lattices consisting of silver nanoparticles with in-plane polarized modes. Eigenvalues of the Wilson loop matrix are employed to distinguish the topological properties of band gaps of our model. The calculation results demonstrate that the proposed model with in-plane polarization supports the obstructed atomic limit phase not only in the middle gap but also in the band gaps that are opened due to the vectorization of in-plane polarizations. The topological edge modes and corner modes are demonstrated by a ribbon supercell and a hexagonal finite-sized system, respectively. To reveal the differences between topological states that appear in different band gaps, we explore the robustness of these corner states by introducing two types of point defects in a finite-sized system. Our work reveals the inherent differences between the topological properties of two-dimensional nanoparticle arrays with in-plane or out-of-plane polarized modes and may extend the application and research of topological plasmonic system.

DOI: 10.1103/PhysRevA.109.023506

I. INTRODUCTION

The topological nature of matters is described by topological invariants which are characterized by quantized number [1,2]. On the boundary of two systems with different topological phases, topological states are formed and robust against defects and impurities due to symmetry protection [3,4]. The robustness renders them promising for applications in many aspects, such as topological insulator laser [5] and electronics and quantum computing [6]. Based on similarity between electronic and photonic systems, the remarkable properties of topological states obtained the rapid development in some photonic topological insulators [4,7].

Plasmonic systems is a widely employed platform to bind the propagation and field distribution of light on the nanoscale [8–11]. The plasmonic systems with topological effects provide a new path to precisely control light on the nanoscale [10,12]. Nanoparticle arrays is a class of plasmonic systems which can enhance and localized the electromagnetic waves due to localized surface plasmon (LSP) resonances [13,14]. The optical properties of the nanoparticle arrays, such as the resonance frequency and band structure, can be adjusted flexibly by the individual nanoparticle elements and the lattice constants of the nanoparticle arrays [11,13]. Based on the coupled dipole method (CDM), the interaction between nanoparticles is simplified to form a concise eigenvalue problem [11,15]. Especially in a deep subwavelength regime, where the quasistatic approximation (QSA) can be applied, the nanoparticle arrays can be considered as a tight-binding model when we only include the nearest-neighbor interaction [15–17]. Therefore, topological effects in nanoparticle arrays have been widely studied, including one- [18] and two-dimensional (2D) [19] Su-Schrieffer-Heeger models, kagome [16,20] and honeycomb [10,15,17] plasmonic nanoparticle arrays. Naturally, the interaction between nanoparticles can be decoupled into independent out-of-plane and in-plane polarizations [14,15]. In the current literature, most discussions about the topological properties in plasmonic nanoparticle systems focus on the out-of-plane modes. However, the topological effects of in-plane polarized modes also deserve some attention. Different from out-of-plane modes, the interaction of point dipoles between nanoparticles is anisotropic due to the vectorization of in-plane polarizations. This is similar to the interactions between neighboring sites in graphene with the p_{xy} orbital [21]. Therefore, it is natural to ask whether the in-plane mode can lead to new topological phenomena that differ with the out-of-plane mode in breathing honeycomb lattices.

In this paper, we investigate the topological effects of breathing honeycomb plasmonic nanoparticle arrays and focus on the in-plane polarizations mode. The breathing honeycomb plasmonic lattice is constructed by silver sphere nanoparticles. The band structures of this model are represented in three forms: with QSA, without QSA and eigenpolarizability [22]. The analysis of band structure shows that the band inversion takes place not only in the middle gap but also in the first (last) gap, topological edge states emerge in both kinds of gap. The coexistence of topological states in different band gaps is one of the most significant differences between the topological properties of in-plane modes and out-of-plane modes. Wilson loops, which describe the evolution of Wannier centers around closed loops in the Brillouin zone, are used to distinguish the topological characters of our model with different lattice configurations [23–25]. We calculate the Wilson loop matrix in the QSA due to that we are in a deep subwavelength regime to operate our model [17,20]. Next, we reveal the topological edge modes by a ribbon supercell

*whz765126390@163.com

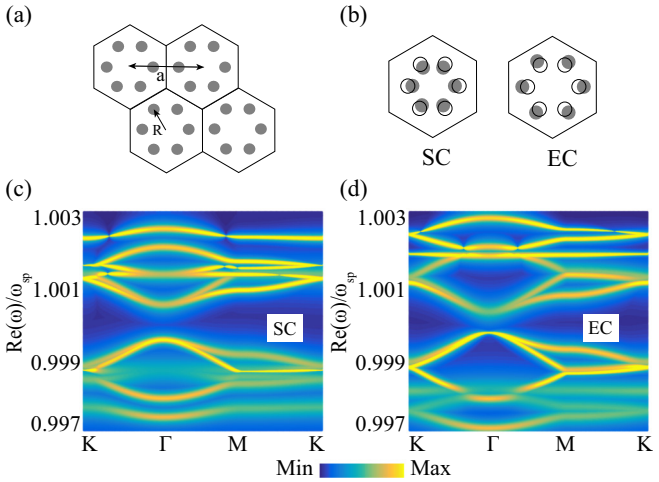

FIG. 1. Schematic diagram of unit cells and band structures. (a) Breathing honeycomb plasmonic nanoparticle arrays. (b) Shrunken cell and expanded cell, black edged hollow circles correspond to the place $m = 1$. (c), (d) Intensity plot of $\mathrm{Im}[\lambda^{-1}(\omega)]$ of SC and EC, respectively.

and a hexagonal finite-sized system, the eigenvalue spectrum is calculated, respectively. We further introduce two kinds of point defects to explore the robustness of these edge states and the differences between the corner states in the middle gap and first (last) gap.

II. MODEL AND BAND STRUCTURES

The honeycomb plasmonic system we consider here consists of identical metallic sphere nanoparticles, as shown in Fig. 1(a), the unit cells containing six nanoparticles of radius r arranged in a hexagon form a triangular lattice with lattice constant a. We set the spacing R between two nearest-neighbor nanoparticles in a unit cell is large enough compared with $r(R > 3r)$, then the nanoparticles can be treated as point dipoles and higher-order resonances can be neglected [26]. Using the method of discrete dipole approximation [14], a coupled dipole equation that describes the dipole moment of our 2D model can be written as

$$\frac{1}{\alpha(\omega)}\mathbf{P}_i = \mathbf{E}_i + \sum_{i\neq j}\mathbf{G}(\mathbf{d}_j, \mathbf{d}_i)\mathbf{P}_j, \tag{1}$$

where $\mathbf{P}_i$ and $\mathbf{d}_i$ are the dipole moment and position of the ith nanoparticle in the array, respectively. $\mathbf{E}_i$ is the external electric field in $\mathbf{d}_i$. $\mathbf{G}$ is the dyadic Green's function that describes the interaction between the jth and the ith dipole. For the in-plane polarized mode, it can be written as

$$\mathbf{G}(\mathbf{d}_j, \mathbf{d}_i) = \left[\frac{1}{d^3}(-\mathbf{I} + 3\mathbf{n}\otimes\mathbf{n}) + \frac{ik}{d^2}(\mathbf{I} - 3\mathbf{n}\otimes\mathbf{n}) + \frac{k^2}{d}(\mathbf{I} - \mathbf{n}\otimes\mathbf{n})\right]e^{ikd}, \tag{2}$$

where $d = |\mathbf{d}_j - \mathbf{d}_i|$, $\mathbf{n}$ is the unit vector between the two nanoparticles, $k = \sqrt{\epsilon_b}\omega/c$ is the wave number of the incident wave in the embedding medium with permittivity ϵ_b. $\alpha(\omega)$ in Eq. (1) represents the dipole polarizability which in the quasistatic approximation can be written as

$$\alpha_Q(\omega) = \frac{\epsilon(\omega) - \epsilon_b}{\epsilon(\omega) + 2\epsilon_b}r^3, \tag{3}$$

the dielectric function of the nanoparticles follows the Drude model $\epsilon(\omega) = \epsilon_\infty - \omega_p^2/(\omega^2 + i\omega\gamma)$. In this work, we consider silver nanoparticles with $r = 5$ nm, $\epsilon_\infty = 5$, $\omega_p = 1.36 \times 10^{16}$ rad/s, and $\gamma = 5.88 \times 10^{13}$ rad/s, embedded in air with $\epsilon_b = 1$. Taking the radiative effects into account, the modified dipole polarizability called the radiative correction can be derived as [14]

$$\alpha(\omega) = \frac{\alpha_Q}{1 - \frac{2i}{3}k^3\alpha_Q}. \tag{4}$$

The proposed unit cells are shown in Fig. 1(b). Specifically, there are shrunken cells (SCs) and expanded cells (ECs), which means that the nanoparticles in the unit cell are displaced toward (SC) or away from (EC) the center of the unit cell. We set $R = \frac{1}{3}ma$, lattice constant $a = 120$ nm, SC and EC correspond to $m = 0.88$ and $m = 1.12$, respectively. The band structures will be described in three forms. We start by calculating the eigenpolarizability using the eigen response theory [22,27]. The band structures can be calculated by solving the following non-Hermitian eigenequation based on the self-consistent coupled dipole equation:

$$\left[\frac{1}{\alpha(\omega)}\mathbf{I} - \mathbf{H}(\mathbf{k}, \omega)\right]\mathbf{p} = \lambda(\omega)\mathbf{p}, \tag{5}$$

where $\mathbf{H}(\mathbf{k}, \omega)$ is given by

$$H_{ij} = \begin{cases} \sum_{\mathbf{X}}\mathbf{G}(\mathbf{d}_j, \mathbf{d}_i + \mathbf{X})e^{i\mathbf{kx}}, & i \neq j \\ \sum_{\mathbf{X}\neq\mathbf{0}}\mathbf{G}(\mathbf{0}, \mathbf{X})e^{i\mathbf{kx}}, & i = j, \end{cases} \tag{6}$$

where $\mathbf{k}$ is the Bloch wave vector, $\mathbf{X}$ represents the triangular lattice site and the nearest-neighbor approximation is considered in this paper. However, it is difficult to find the corresponding ω numerically under fixed $\mathbf{k}$ because of the complex form of the dyadic Green's function. Instead, we calculate the eigenvalue of Eq. (5) with $(\mathbf{k}, \omega) = (\mathbf{k}_e, \omega_e)$, where $\mathbf{k}_e$ and ω_e go through the first Brillouin zone and frequency near the surface-plasmon resonance $\omega_{sp} = \omega_p/\sqrt{\epsilon_\infty + 2\epsilon_b}$, respectively. In eigen response theory, the total power loss in the system is proportional to $\mathrm{Im}[\lambda^{-1}(\omega)]$, the band structure can be included by the peak of $\mathrm{Im}[\lambda^{-1}(\omega)]$ which indicates the resonant frequency of the plasmonic system. The $\mathrm{Im}[\lambda^{-1}(\omega)]$ of SC and EC are shown in Figs. 1(c) and 1(d), respectively. Another method is to approximately linearized the dyadic Green's function with $\omega = \omega_{sp}$ in Eq. (2) since the Green's function changes slowly with ω while the polarizability changes rapidly with ω for small nanoparticles in the subwavelength regime [10]. Then, the band structures can be calculated by solving

$$\det\left[\frac{1}{\alpha(\omega)}\mathbf{I} - \mathbf{H}(\mathbf{k}, \omega_{sp})\right] = 0. \tag{7}$$

We plot the results in Appendix A, which are highly consistent with the peak of $\mathrm{Im}[\lambda^{-1}(\omega)]$, suggesting that the linearized dyadic Green's function is precise enough to describe our models.

The band structures in Fig. 1 and Appendix A indicate that a doubly degenerate Dirac cone near ω_{sp} open and close and reopen when we deform the unit cell from SC to EC. This is similar to the out-of-plane mode of breathing plasmonic honeycomb lattices [17]. In addition, global band gaps also appear in other places in both SC and EC by opening the degenerate band on the Brillouin-zone boundary M-K lines. In the next section, the topological properties of these band gaps will be discussed in detail, especially the differences with the topological states in the out-of-plane mode.

III. TOPOLOGICAL CHARACTERISTICS AND SPECTRA OF EDGE STATES

The topological characteristics of bands can be distinguished by the eigenvalues of their Wilson loop matrix which providing the information about the evolution of the Wannier centers around closed paths in the Brillouin zone. We give the Wilson loops in the QSA which has been widely used in topological plasmonic systems [15,16,20], then the eigenequation of Eq. (5) can be simplified down to a Hermitian eigenvalue problem. More details about the Wilson loops are given in Appendix B. Before calculating the Wilson loops, we give the band structure of our models in the QSA, as shown in Appendix A. The results show that the opening and closing of the band gaps is consistent with the red lines despite slight deformation.

As shown in Fig. 1, a gap between the sixth and seventh band (we call it second gap) is opened in both SC and EC. However, the first (third) gap appear between the first (last) and second (last but one) band in SC while appear between the second (last but one) and third (last but two) band in EC. We calculate the Wilson loops as presented in Fig. 2. In Figs. 2(a) and 2(b), the Wilson loops of SC distribute near zero, indicating the triviality of the gaps. However, for the EC, the Wilson loops move to $\pm\pi$ obviously, as shown in Figs. 2(c) and 2(d), which is representative of an obstructed atomic limit phase [16,23]. Note that the first and third gap have the same topological properties because of the chiral symmetry [28].

Next, we show that the inversion of modes take place upon deforming the unit cell from SC to EC in both first and second gap. The band modes are determined by calculating the dipole momentum distributions with the eigenstates in a unit cell [8]. Different with out-of-plane mode which is similar to a scalar model [10,16], the dipole moments of in-plane mode are in-plane vectors as shown in Figs. 2(e) and 2(f). The inversion of modes can be identified by these in-plane vectors. For the second gap, Fig. 2(f), the dipole moments from band five to band eight at the Γ point indicate the inversion between the double degenerate points above and below the second gap for the SC and EC. For the first gap, the inversion happens between band one and band three, as shown in Fig. 2(e). This kind of band gap that is far from ω_{sp} is difficult to be opened and appears only in the SC in out-of-plane modes [10,17]; however, they are supported in both SC and EC in the in-plane modes, as shown in Fig. 1 because of the anisotropic interactions of in-plane polarized modes [16,21]. In fact, this kind of band gap can also be created in scalar systems by breaking the C_6 symmetry [29].

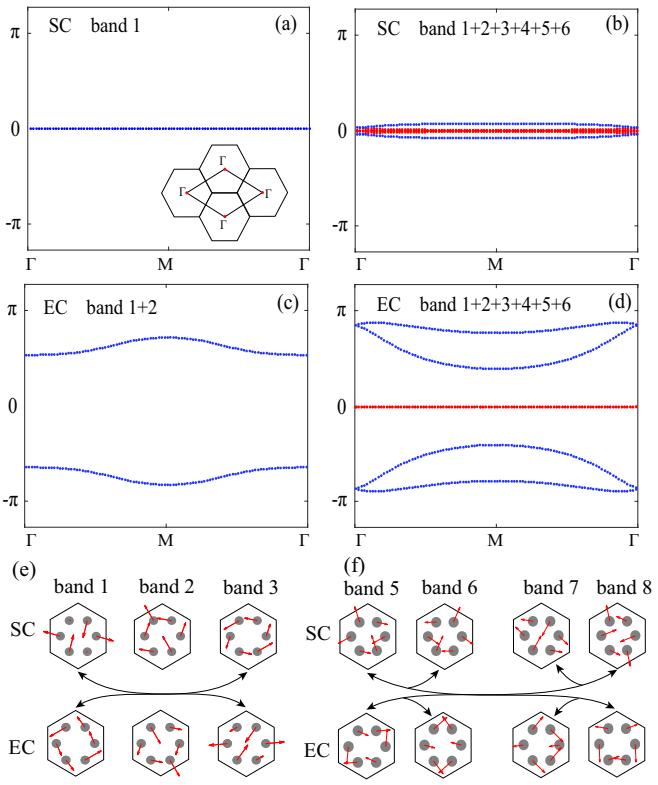

FIG. 2. Wilson loop eigenvalues of the SC (a) for the first gap and (b) for the second gap. The same for the EC (c) first gap and (d) second gap. The red lines in panels (b) and (d) are respectively quadruple and double degenerate. (e) Mode of band 1 to 3 at M. (f) Mode of band 5 to 8 at Γ. The red arrow in panels (e) and (f) represents the dipole moments of the corresponding nanoparticle.

To verify the topological properties described above, we set up a ribbon consisting of twelve ECs. The projected band structure along the k_y direction of this ribbon is shown in Fig. 3(a). The result indicates that there are two and one lines appearing in the second and first (third) gap, respectively. These lines are double degenerate edge states, for example, C1 and C2. The electric-field intensity distribution of the edge states are shown in Fig. 3(b). The edge modes appearing in the second gap (B, C1, and C2 in Fig. 3) are near ω_{sp} and are typical cases of topological edge states that are protected by chiral symmetry [24,30]. The edge modes appearing in the first (third) gap (A and D) are topologically protected by mirror symmetries which have been studied extensively in topological photonic crystals [31]. The difference in the symmetry of the two kinds of topological states leads to the differences of their robustness against defects, which will be discussed in detail in Sec. IV.

IV. TOPOLOGICAL CORNER MODES AND ROBUSTNESS

To investigate corner modes, we use the ECs to construct a hexagonal finite-sized system with a side length of four ECs. The eigenmodes of this finite-sized system are symmetric about the ω_{sp}, as shown in Fig. 4(a), because of the chiral symmetry [30]. There are three groups of edge modes with six corner states in each group corresponding to the three gaps of EC's band structure, respectively. We label them as group A,

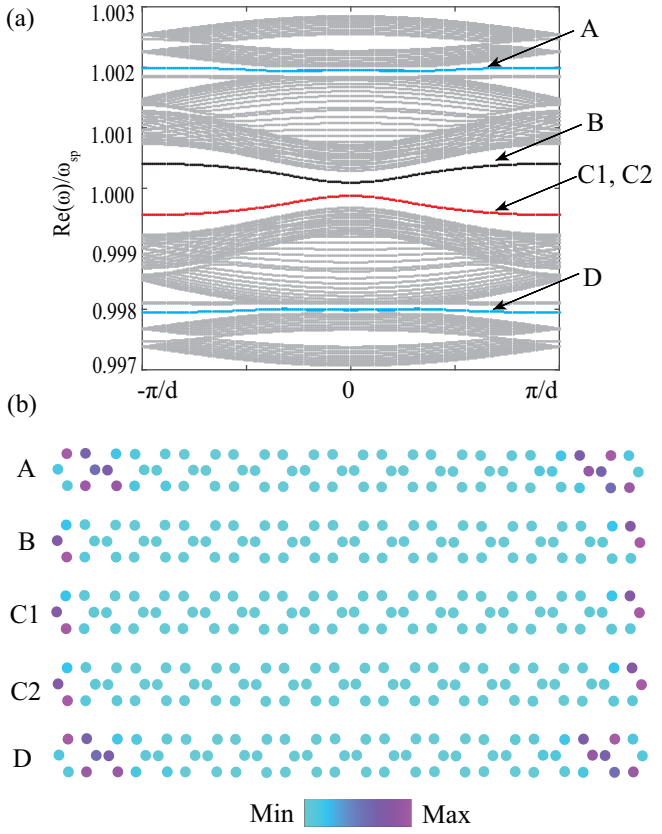

FIG. 3. (a) Projected band structure of a ribbon consisting of twelve ECs. (b) The electric-field intensity distribution of typical edge states of this ribbon. C1 and C2 are double degenerate edge modes.

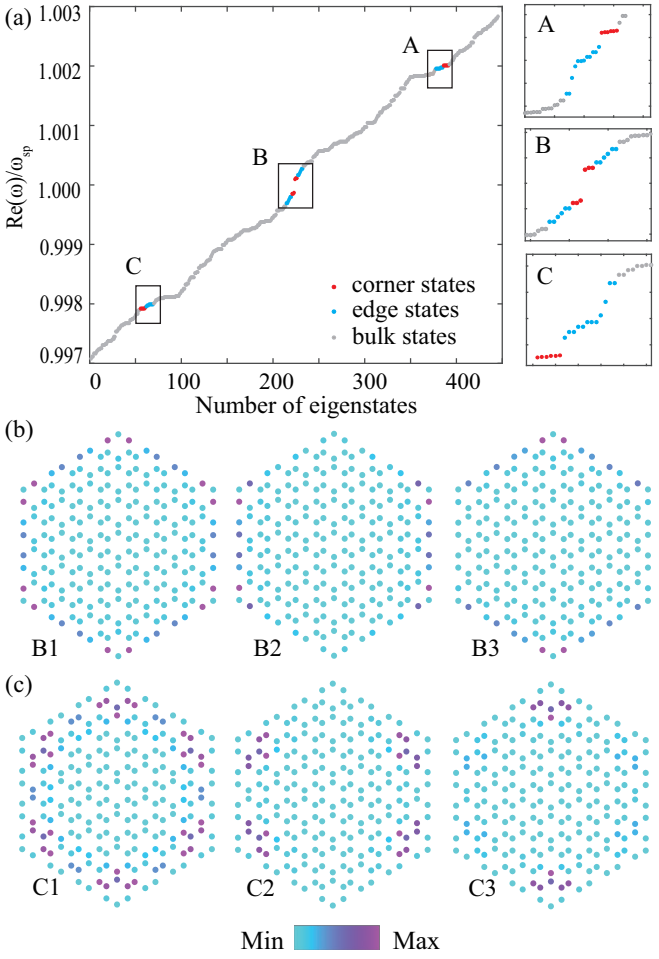

FIG. 4. (a) The eigenvalue spectrum of a hexagonal finite-sized system with a side length of four ECs. The right-hand plots are zoom-in structures of A, B, and C in panel (a). (b), (c) The three types of corner states in B and C, respectively.

B, and C, as shown in Fig. 4(a). In each group, the corner modes can be divided into three types: concentrate at two, four, or six corners of the hexagonal finite-size system, and there are two of each type. The three types of corner states in groups B and C are shown in Figs. 4(b) and 4(c), respectively.

To reveal the differences between topological states that appear in different band gaps, the robustness of the corner modes is explored by two kinds of defects. First, we remove one nanoparticle at exactly the corner of the above hexagonal finite-sized system (defect i). This defect breaks the geometrical C_6 symmetry, however, the mirror symmetry and chiral symmetry, which protect the topological states of group A (C) and B, respectively, remain. As a result, the corner modes in group A (C) and B are robust against this defect. Another kind of defect can be created by removing the nanoparticle next to the corner of the complete hexagon system above (defect ii). This defect breaks the C_6 symmetry and mirror symmetry but has little effect on the chiral symmetry, which can be illustrated by the symmetry of eigenvalue spectrum about ω_{sp}, as shown in Fig. 5(a). Therefore, the corner states in group A (C) and B should suffer different robustness against this kind of defects.

As shown in Fig. 5(a), *i* and *ii* represent the eigenvalue spectrum of the above finite-sized system with the defect *i* or *ii*, respectively. In Figs. 5(b) and 5(c), we plot the electric-field intensity distribution of those corner states that we care about. The other corner states concentrated at four or six corners of the finite-sized system have no significant difference with the original ones and are not shown here. As we can see from *iBa*, *iBb* and *iiBa*, *iiBb*, the electric-field intensity of the corner states appearing in the middle gap similarly distribute against the two kinds of defects. However, they are different between the finite-sized system with defect *i* or defect *ii* when it comes to group A (C). Specifically, the corner states of defect *i*, *iCa* and *iCb* in Fig. 5(c), are similar to the original ones, as shown by C3 in Fig. 4(c), because of the remain of mirror symmetry under defect *i*. However, the two corner states of defect *ii* are concentrated at one or three corners of the finite-sized system, as shown in Fig. 5(c) *iiCa* and *iiCb* since the mirror symmetry that protects the corner states is broken and new symmetrical characteristics are met after this kind of defect is created.

V. CONCLUSION

In conclusion, we have presented a study of topological edge modes in breathing honeycomb plasmonic nanoparticle arrays with the in-plane polarized mode. Different with the out-of-plane mode, topological edge states can be maintained not only in the middle gap, but also in the first

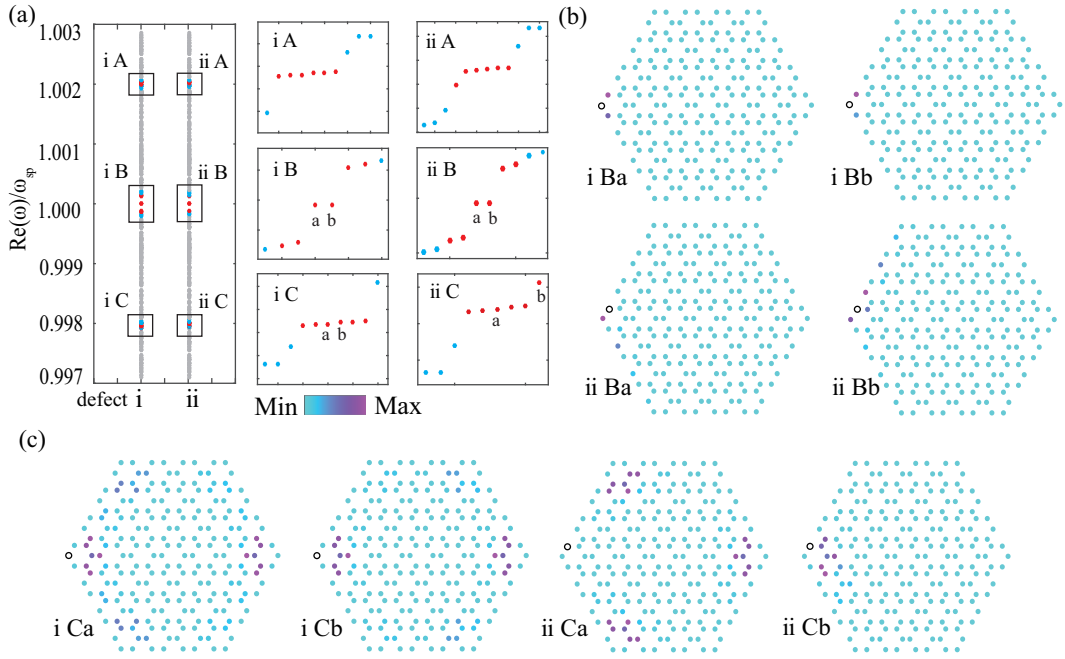

FIG. 5. (a) The eigenvalue spectrums of the hexagonal finite-sized system with defect *i* or *ii*. The middle and right-hand plots are zoom-in structures of corresponding areas in panel (a). (b) The electric-field intensity distribution of the corner states in group B against defect *i* or *ii*. (c) The electric-field intensity distribution of the corner states in group C against defect *i* or *ii*. The black edged hollow circle in panels (b) and (c) corresponds to the place of point defects.

(last) gap of EC. The calculation of Wilson loops indicates that the topological effects in both kinds of band gaps are the result of an obstructed atomic limit. The edge modes appearing in the middle gap are topologically protected by chiral symmetry while the edge modes appearing in the first (third) gap are topologically protected by mirror symmetries. As a result, these edge modes show different robustness against point defects. Our work indicates the intriguing differences between the topological states in breathing honeycomb nanoparticle arrays with in-plane or out-of-plane polarized modes and provides a new path for the coexistence of topological states in a plasmonic system which could have potentially importance and novel applications in nanophotonics.

ACKNOWLEDGMENTS

This work was supported by Shenzhen Science and Technology Program (Grant No. JCYJ20210324132416040), Guangdong Provincial Nature Science Foundation (Grant No. 2022A1515011488), and the National Key Research and Development Program of China (Grant No. 2022YFB3603204).

APPENDIX A: BAND STRUCTURE WITH LINEARIZED DYADIC GREEN'S FUNCTION

We have calculated the Band structures by solving Eq. (7). Figure 6 shows the results.

APPENDIX B: THE CALCULATION OF WILSON LOOPS

The Wilson loops in this work involve a group of degenerate bands. It can be defined as

$$W(k_i) = -\mathrm{Im}\left[log\left(\prod_{k_j} S_{(k_i,k_j),(k_i,k_{j+1})} \right) \right], \qquad \text{(B1)}$$

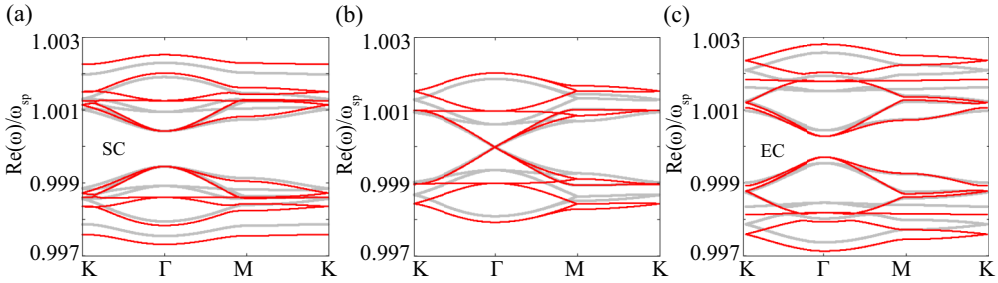

FIG. 6. Panels [(a)–(c)] show the band structure of SC, $m = 1$, and EC, respectively. The red lines and gray lines are the band structure calculated with and without QSA, respectively.

where the S_{k_1,k_2} is the overlap matrix and can be expressed as

$$S_{k_1,k_2} = \begin{bmatrix} \langle u^1_{k_1} | u^1_{k_2} \rangle & \langle u^1_{k_1} | u^2_{k_2} \rangle & \cdots \\ \langle u^2_{k_1} | u^1_{k_2} \rangle & \langle u^2_{k_1} | u^2_{k_2} \rangle & \cdots \\ \vdots & \vdots & \ddots \end{bmatrix}, \tag{B2}$$

where $u^n_{k_{1,2}}$ is the periodic part of the Bloch wave function, k_1 and k_2 are the Bloch wave vectors, and n is the index of degenerate bands. The eigenvalues of W give information about the position of the Wannier centers.

[1] Z. Song, Z. Fang, and C. Fang, $(d-2)$-dimensional edge states of rotation symmetry protected topological states, Phys. Rev. Lett. **119**, 246402 (2017).

[2] W. A. Benalcazar, B. A. Bernevig, and T. L. Hughes, Electric multipole moments, topological multipole moment pumping, and chiral hinge states in crystalline insulators, Phys. Rev. B **96**, 245115 (2017).

[3] F. Liu and K. Wakabayashi, Novel topological phase with a zero Berry curvature, Phys. Rev. Lett. **118**, 076803 (2017).

[4] T. Ozawa, H. M. Price, A. Amo, N. Goldman, M. Hafezi, L. Lu, M. C. Rechtsman, D. Schuster, J. Simon, O. Zilberberg, and I. Carusotto, Topological photonics, Rev. Mod. Phys. **91**, 015006 (2019).

[5] Y. V. Kartashov and D. V. Skryabin, Two-dimensional topological polariton laser, Phys. Rev. Lett. **122**, 083902 (2019).

[6] J. S. Van Dyke and D. K. Morr, Controlling the flow of spin and charge in nanoscopic topological insulators, Phys. Rev. B **93**, 081401(R) (2016).

[7] L.-H. Wu and X. Hu, Scheme for achieving a topological photonic crystal by using dielectric material, Phys. Rev. Lett. **114**, 223901 (2015).

[8] C. Cherqui, M. R. Bourgeois, D. Wang, and G. C. Schatz, Plasmonic surface lattice resonances: Theory and computation, Acc. Chem. Res. **52**, 2548 (2019).

[9] D. F. Kornovan, R. S. Savelev, Y. Kivshar, and M. I. Petrov, High-q localized states in finite arrays of subwavelength resonators, ACS Photonics **8**, 3627 (2021).

[10] P. Matthew, V. C. Richard, A. M. Stefan, G. Vincenzo, and A. H. Paloma, Exciting pseudospin-dependent edge states in plasmonic metasurfaces, ACS Photonics **6**, 2985 (2019).

[11] F. Fernique and G. Weick, Plasmons in two-dimensional lattices of near-field coupled nanoparticles, Phys. Rev. B **102**, 045420 (2020).

[12] C.-R. Mann and E. Mariani, Topological transitions in arrays of dipoles coupled to a cavity waveguide, Phys. Rev. Res. **4**, 013078 (2022).

[13] F. J. García de Abajo, *Colloquium:* Light scattering by particle and hole arrays, Rev. Mod. Phys. **79**, 1267 (2007).

[14] Y.-R. Zhen, K. H. Fung, and C. T. Chan, Collective plasmonic modes in two-dimensional periodic arrays of metal nanoparticles, Phys. Rev. B **78**, 035419 (2008).

[15] L. Wang, R. Y. Zhang, M. Xiao, D. Z. Han, C. T. Chan, and W. J. Wen, The existence of topological edge states in honeycomb plasmonic lattices, New J. Phys. **18**, 103029 (2016).

[16] Y. Zhang, R. P. H. Wu, L. Shi, and K. H. Fung, Second-order topological photonic modes in dipolar arrays, ACS Photonics **7**, 2002 (2020).

[17] M. Honari-Latifpour and L. Yousefi, Topological plasmonic edge states in a planar array of metallic nanoparticles, Nanophotonics **8**, 799 (2019).

[18] S. R. Pocock, X. F. Xiao, P. A. Huidobro, and V. Giannini, Topological plasmonic chain with retardation and radiative effects, ACS Photonics **5**, 2271 (2018).

[19] H. Schlömer, Z. Jiang, and S. Haas, Plasmons in two-dimensional topological insulators, Phys. Rev. B **103**, 115116 (2021).

[20] M. Proctor, M. Blanco de Paz, D. Bercioux, A. Garcia-Etxarri, and P. A. Huidobro, Higher-order topology in plasmonic kagome lattices, Appl. Phys. Lett. **118**, 091105 (2021).

[21] C. Wu and S. Das Sarma, $p_{x,y}$-orbital counterpart of graphene: Cold atoms in the honeycomb optical lattice, Phys. Rev. B **77**, 235107 (2008).

[22] K. H. Fung and C. T. Chan, Plasmonic modes in periodic metal nanoparticle chains: A direct dynamic eigenmode analysis, Opt. Lett. **32**, 973 (2007).

[23] S. J. Palmer and V. Giannini, Berry bands and pseudo-spin of topological photonic phases, Phys. Rev. Res. **3**, L022013 (2021).

[24] M. Proctor, P. A. Huidobro, B. Bradlyn, M. B. de Paz, M. G. Vergniory, D. Bercioux, and A. García-Etxarri, Robustness of topological corner modes in photonic crystals, Phys. Rev. Res. **2**, 042038(R) (2020).

[25] M. Blanco De Paz, C. Devescovi, G. Giedke, J. J. Saenz, M. G. Vergniory, B. Bradlyn, D. Bercioux, and A. García-Etxarri, Tutorial: Computing topological invariants in 2D photonic crystals, Adv. Quantum Technol. **3**, 1900117 (2020).

[26] S. A. Maier, P. G. Kik, and H. A. Atwater, Optical pulse propagation in metal nanoparticle chain waveguides, Phys. Rev. B **67**, 205402 (2003).

[27] C. W. Ling, J. Wang, and K. H. Fung, Formation of nonreciprocal bands in magnetized diatomic plasmonic chains, Phys. Rev. B **92**, 165430 (2015).

[28] Z.-Z. Yang, A.-Y. Guan, W.-J. Yang, X.-Y. Zou, and J.-C. Cheng, Surface impedance and generalized chiral symmetry in acoustic higher-order topological insulators, Phys. Rev. B **103**, 214112 (2021).

[29] M. L. N. Chen, L. J. Jiang, Z. Lan, and W. E. I. Sha, Coexistence of pseudospin- and valley-Hall-like edge states in a photonic crystal with C_{3v} symmetry, Phys. Rev. Res. **2**, 043148 (2020).

[30] W. A. Benalcazar and A. Cerjan, Bound states in the continuum of higher-order topological insulators, Phys. Rev. B **101**, 161116(R) (2020).

[31] B.-Y. Xie, H.-F. Wang, H.-X. Wang, X.-Y. Zhu, J.-H. Jiang, M.-H. Lu, and Y.-F. Chen, Second-order photonic topological insulator with corner states, Phys. Rev. B **98**, 205147 (2018).